This manuscript was accepted by Appl. Phys. Lett. Click here to see the version of record.

# Monolayer and thin *h*–BN as substrates for electron spectro-microscopy analysis of plasmonic nanoparticles

Luiz Henrique Galvão Tizei,[1,*] Hugo Lourenço-Martins,[1] Pabitra Das,[1] Steffi Y. Woo,[1] Leonardo Scarabelli,[2,3] Christoph Hanske,[3] Luis M. Liz-Marzán,[3,4] Kenji Watanabe,[5] Takashi Taniguchi,[5] and Mathieu Kociak[1]

[1] *Laboratoire de Physique des Solides, Université Paris-Sud, CNRS-UMR 8502, Orsay 91405, France*
[2] *Department of Chemistry & Biochemistry, University of California, Los Angeles, Los Angeles, California 90095, United States*
[3] *CIC biomaGUNE and Ciber-BBN, Paseo de Miramón 182, 20014 Donostia - San Sebastián, Spain*
[4] *Ikerbasque, Basque Foundation for Science, 48013 Bilbao, Spain*
[5] *National Institute for Materials Science, Namiki 1-1, Tsukuba, Ibaraki 305-0044, Japan*

The influence of four substrates (thin $Si_3N_4$, few layers graphene (FLG) and thin and monolayer *h*–BN) on plasmon resonances of metallic nanoparticles was studied using electron energy loss spectroscopy. *h*–BN monolayer is an excellent substrate for the study of plasmonic particles due to its large bandgap, negligible charging under electron irradiation and negligible influence on plasmon resonances full width at half maximum and peak positions. These effects were evidenced in experiments with gold nanotriangles focusing on dipolar modes. Nanotriangles on *h*–BN exhibit the lowest influence of the substrate compared to $Si_3N_4$ and FLG. In a dataset containing 23 triangles of similar sizes, the dipolar mode was found to have smaller redshifts, sharper peak widths and higher resonance quality factors on *h*–BN, showing that it has nearly no effect on the plasmon absorption properties provided it is free from carbon contamination. However, light emission (cathodoluminescence) decreases as a function of electron irradiation for triangles on *h*–BN, even though the electron energy loss signal stays unchanged. This indicates the creation of non-radiative decay channels.





The local dielectric environment plays an important role in the localized surface plasmon resonance (LSPR) of metal nanoparticles (MNPs).[1–11] Changes in the environment can be used to manipulate their plasmonic response. When the MNP is immersed in a homogeneous dielectric medium, an increase in the local dielectric environment leads, in general, to resonance redshifts. As the environment is symmetric, the comparison to theory is usually simplified. In contrast, when the MNP is placed on a substrate, the symmetry is broken,[5,12,13] leading to more complicated behavior. This complicates the comparison between theory and experiments and the interpretation of fine details observed in optical measurements. Any spectroscopic experiment performed in microscopes to probe plasmons, and specifically for electron microscopes (EM), demands the sample under study to be deposited on some type of substrate. The resulting broken symmetry has significant consequences in the LSPR of the MNP, which is a matter of intensive study.[5,10,12,13] For example, the plasmonic response of Ag cubes on substrates is still not fully understood,[12,13] although theoretical tools have been developed,[14–20] to the point that 3D reconstructions of plasmonic modes is possible.[21] In simplistic picture within the quasistatic limit for small MNPs, image charges in the substrate are induced by electron oscillations associated with the plasmon modes.[6] The magnitude of the image charge depends on the refractive index of the substrate. Interaction of the excited plasmon modes of the nanoparticle and the image charges modifies the overall response.[6] Such models can be extremely precise for symmetrical substrates, as demonstrated by optical scattering experiments.[22]

Current standard substrates for EM experiments have known drawbacks. Thin $Si_3N_4$ (typically 15 nm) induces large redshifts of plasmon resonances and is prone to charging in the EM, inducing extra geometric aberrations on the electron beam. Few layers graphene (FLG) is conductive, avoiding the charge-induced problems, and leads to smaller redshifts. However, the lack of a bandgap introduces extra absorption at the plasmon energies and as well as plasmon damping (broader peak widths).

In this context, *h*–BN is a promising candidate, a material with a wide bandgap which has been recently shown to be a good substrate for experiments with 2D materials, including graphene and transition metal dichalcogenides[23], for enhancing surface-enhanced Raman spectroscopy[24] and as an excitation medium for cathodoluminescence.[25] *h*–BN has a larger dielectric constant in comparison to $Si_3N_4$. Therefore, a thin *h*–BN layer or possibly a monolayer should be used to minimize its influence on plasmonic resonances. Thin *h*–BN is much less prone to charging effects than 15 nm $Si_3N_4$. Moreover, the use of a monolayer of *h*-BN as a substrate may present further technological advantages, being malleable, transparent and capable of offering protection (fully covering a surface) against oxidation in a sandwich configuration under ambient conditions[26,27].

To determine the utility of *h*–BN for plasmonics in EM studies we used a combination of spectroscopic techniques and theoretical modeling to explore the effects of four substrates on plasmonic nanoparticles: 1) 15 nm thick $Si_3N_4$ membranes, 2) FLG, 3) monolayer *h*–BN and 4) thin *h*–BN. The first two have been explored extensively in plasmonic studies in EM.[9] Up to now, *h*–BN has not been considered as a substrate for plasmonics, possibly due to the fact that a thick layer of this material is prone to charging. We show that thin or monolayer *h*–BN are more appropriate than current standard sub-

This manuscript was accepted by Appl. Phys. Lett. Click here to see the version of record.

strates for plasmonic studies in EM, provided it is free from carbon contamination.

According to well-known models, we expect that a substrate with a higher dielectric constant will induce a larger plasmon redshift and an increase in its full width at half maximum (FWHM). The thickness of the substrate must necessarily influence these quantities, as the field penetration in the substrate will decrease for thinner materials. Therefore, a quantity taking into account the magnitude of the dielectric constant and thickness has to be considered, similarly to the effective refractive index used when calculating optical modes in photonic crystals. In short, we expect that the reduced thickness of the *h*–BN monolayer (∼0.3 nm) will reduce the influence of its higher dielectric constant, leading to smaller redshifts and narrower FWHM in comparison to $Si_3N_4$. In fact, as we observed, even a thin film of h-BN has an effect smaller than that of other substrates. Theoretically, this transition cannot be analyzed with available methods, as described for $Si_3N_4$ in the text. For example, in BEM (boundary element method) charges and dipoles are calculated at the boundaries between the metal particles and dielectric media. Including these boundaries is complicated, even for "thick" substrates and no definitive method exists for atomically thin materials. For our calculations we used the MATLAB toolbox MNPBEM.[17]

In our experiments we used gold (Au) nanotriangles as model MNPs, with average edge size of 80 nm and thickness 34 nm (4% and 25% standard deviation, which would lead to plasmon shifts of the order of 100 meV at the maximum, far smaller than the shifts observed experimentally (Supplementary material, SM S1 and Table S1). Nanotriangles were synthesized using a seed mediated protocol and their small dispersion in size allowed us to analyze MNPs with the same nominal size in all three substrates.[28] The 15 nm nominal $Si_3N_4$ and FLG substrates were purchased (Ted Pella). The monolayer *h*–BN substrate was produced by transferring a monolayer of *h*–BN (described in the SM) grown by CVD on copper (purchased from Graphene Supermarket) onto a TEM molybdenum grid (quantiFOIL) containing a thick carbon film with a 1 $\mu$m hole array. Thin *h*–BN (thickness < 10 nm) flakes were produced by liquid exfoliation of pure *h*–BN high-temperature-high-pressure monocrystals using isopropanol (15 minutes of sonication). The resulting solution was drop cast on lacey carbon films suspended on copper grids. The MNPs were deposited by simple drop casting on top of each substrate after dilution of the solution in deionized water. Two spectroscopy techniques were used in a STEM: electron energy loss spectroscopy (EELS, a nanoscale equivalent of optical extinction[4,8,9] in the near-visible range) and cathodoluminescence (CL, a nanoscale equivalent of optical scattering for plasmonics[9]). The small electron probe available in STEMs ensures high spatial resolution. All EELS experiments were performed on a Nion UltraSTEM 200 operated at 60 keV with an electron beam of about 1.2Å (few tens of pA beam current, 34 mrad convergence semi-angle and 10 mrad spectrometer collection semi-angle). The electron beam energy spread (FWHM) was 260 meV. CL experiments were performed in a VG HB 501 microscope operated at 60 keV or 100 keV with an electron beam of about 1 nm (few hundreds of pA beam current and 15 mrad convergence semi-angle). EELS data were deconvolved using a Richardson-Lucy algorithm.[29] Light was collected using a Mönch CL system for STEMs from Attolight.[30] In STEM experiments MNPs are located using high angle annular dark field (HAADF) images, in which the intensity is proportional to the projected atomic number along the beam path (to a first approximation the intensity is proportional to $Z^n$, where $n$ depends on the detector collection angle[31]). Spectroscopic data were acquired in hyperspectral mode: the beam was scanned on the zone of interest and at each beam position a spectrum (EELS or CL) was acquired, leading to a 3D datacube. Along with each hyperspectral image an HAADF image was acquired in parallel, allowing a direct correlation between the MNPs position and its plasmonic modes.

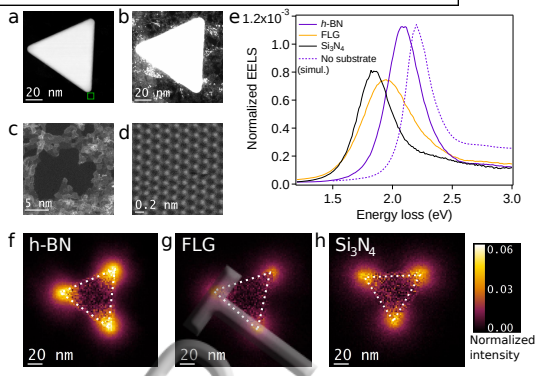


FIG. 1. (a) HAADF image of a gold triangle on *h*–BN substrate. The measured side length of the triangle is 83 nm. The error in length is ±2.5 nm. (b) Same HAADF image as in (a) but with a different contrast for better visibility of the substrate. (c,d) Representative low magnification and high magnification images of the *h*–BN substrate. The darker part of the image in (c) is a monolayer of *h*–BN. (d) is the magnified image of a monolayer region (e) EEL spectra acquired from one corner (in the HAADF image of (a)) of the nanoparticle, when the nanoparticle is placed on different substrates e.g $Si_3N_4$, thin FLG and *h*–BN. The violet dotted curve is the simulated EEL spectra for a free standing gold triangle of the same dimension as in the experiments. (f,g,h) electron energy loss map at resonance energy when the particle is placed on *h*−BN, FLG and $Si_3N_4$.

brighter regions are thicker due to the presence of carbon-containing residue from the *h*-BN monolayer transfer process to the electron microscopy support grid. To confirm the presence of monolayer *h*–BN high resolution imaging was used, as exemplified in Figure 1(d). Brighter dots correspond to nitrogen atoms, while the darker ones to boron.

Different Au nanotriangles were measured for each substrate. In Figure 1 (e-h) we present three triangles with similar sizes (83, 83, 84 nm edge length) deposited on *h*–BN, FLG and 15 nm thick $Si_3N_4$. EELS spectra in the 1.2 eV to 3.0 eV range are shown in Figure 1 (e) acquired with the electron beam at one of the tips of each triangle (marked in green for the *h*–BN sample in Figure 1 (a). For comparison, we also included the MNPBEM simulated EEL spectra for a gold triangle of the same dimensions as used in our experiments in vacuum. Spectra were normalized to the zero-loss peak.

First of all, a shift of the dipolar mode to lower energies can be clearly seen from the theoretical calculation in vacuum (2.22 eV) to the substrates: *h*–BN (2.08 eV), FLG (1.98 eV) and 15 nm $Si_3N_4$ (1.84 eV). These values match our qualitative expectations, considering for example an effective medium model. The higher dielectric constant of *h*–BN than Si3N4 is counterbalanced by the reduced monolayer thickness, and hence, the lower electric field penetration in the dielectric leads to a reduced effective dielectric constant in *h*–BN. However, compared to our MNPBEM calculation, even the *h*–BN dipolar mode appears at lower energy (0.12 eV redshift). The shoulders at higher energy can be attributed to hexapolar modes,[32] which are not easily distinguishable in the shown spectra. Here, we focus on the dipolar mode of MNPs. All of our conclusions can be extended to higher order modes e.g. edge modes[32] or breathing modes.[33,34]

Considering the FWHM of the dipolar modes, we observed 0.16 eV in vacuum (theory), 0.30 eV for *h*–BN, 0.32 eV for $Si_3N_4$ and 0.43 eV for FLG. Our experiments were performed with an electron beam with an energy spread of about 0.26 eV (0.15 eV after deconvolution). Variations below this value, which appear after spectra deconvolution, are hard to quantify. However, the FWHM of the dipolar mode on FLG is larger, indicating a decrease in plasmon total lifetime. Surface plasmons lifetimes have been measured using EELS data fitting.[35] By comparing the FLG spectrum with those of the other substrates, we can see that damping effects play an important role.

Although substrates are routinely included in calculations, their effects are simulated only qualitatively. For example, even in our attempt to minimize substrate effects, a substantial redshift of 0.12 eV is still observed. This could be an effect of residual carbon contaminants on and around the nanoparticles (Figure 1 (b)), error in the particle geometry (triangle edge roundness, for example), or some elements that we are missing in the model. The total effect is stronger than what we expected qualitatively, stressing the problem of calculating the effect of atomically thin substrates in plasmonics.

Figure 1(f-h) shows the experimental EELS plasmon maps for *h*–BN, FLG and $Si_3N_4$ substrates respectively. Filtered images were produced by integrating the scattered intensities at a 200 meV energy range centered on the plasmonic dipole mode peak. For these reasons, energy filtered maps are also normalized. As already observed in the spectra in Figure 1(e), the total EELS intensity of the dipolar mode is higher for the triangle on the *h*–BN substrate (as evidenced in the normalized intensity maps). The decay of the dipolar mode intensity away from the triangles' tip cannot be distinguished between the three measurements.

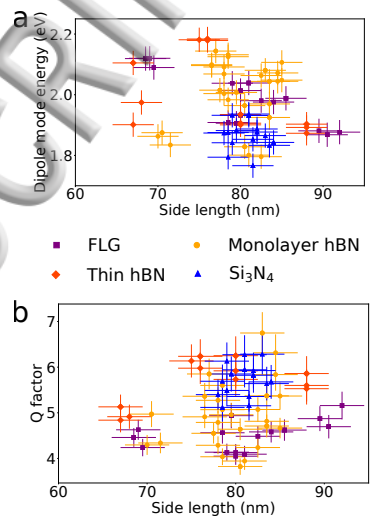


FIG. 2. (a) Dipolar mode peak energy and (b) Q factor as a function of triangle side for 23 triangles on different substrates: monolayer *h*–BN, thin *h*–BN, FLG and $Si_3N_4$.

These three triangles are extreme cases of a general trend observed in a larger dataset. The energy of the dipole peak as a function of the side length of 23 triangles is shown in Figure 2(a). For each triangle, the dipole peak energy for the three vertices is presented. These energies, along with the associated FWHM were measured by fitting a Gaussian to each spectrum, as described in the S2. As described before, resonances in *h*–BN occur at higher energies. However, a large dispersion in energy was observed. In some cases, the dipolar mode of triangles with similar sizes show comparable energies on *h*–BN and on $Si_3N_4$. This occurs due to the presence of carbon contaminants on the surface of the triangles (from the synthesis) and on the *h*–BN monolayer (from the monolayer transfer). To avoid some of this extraneous contamination, we considered thin hBN crystals (below 10 nm thickness, as estimated from EELS). For the thin flakes, the results are consistent with what was observed using hBN monolayers. Finally, the FWHM observed for all triangles (S3) also follow the general trend (sharper peaks for hBN and $Si_3N_4$ and broader for FLG). Thin *h*–BN shows FWHM sharper than those in monolayer

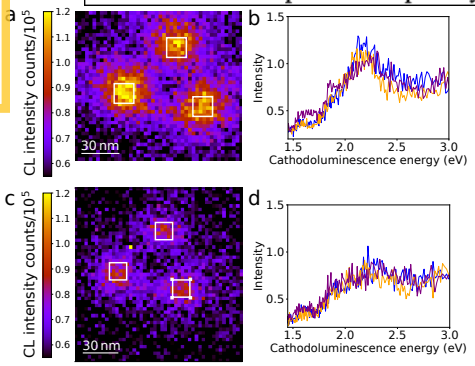


FIG. 3. Nanotriangle on *h*–BN monolayer (a-b) CL intensity map filtered at the plasmon peak (from 1.7 eV to 2.3 eV) and spectra for the first hyperspectral image. (c-d) Same information after the triangle had been illuminated by the electron beam. The color scale in (a-c) and the ordinate axis in (b-d) are identical. The three spectra in (b-d) were integrated at each of the three vertices.

*h*–BN due to smallar quantities of contaminants on its surface. The combination of increase energy and reduced FWHM leads to higher quality factor (Q, the ratio of the resonance energy and its FWHM) on *h*–BN substrates (Figure 2(b)). As a summary, thin *h*–BN has appealing properties compared to the other substrates: contrary to $Si_3N_4$, the best solution in EM at the moment, they are likely to induce smaller red-shifts (related points being statistically in the higher energy part of Figure 2(a)), while keeping a FWHM comparable to the $Si_3N_4$ but much lower than FLG. In Figure 2(a), the expected redshift as a function of increasing particle size is clearer for the $Si_3N_4$ substrate in contrast to the *h*–BN substrates. This is because of carbon contaminants which may also induce redshifts in the plasmonic resonances.

In the whole dataset, variations between the peak energy of the three vertices were observed (from tens to hundreds meV). These variations can again be explained by the presence of varying quantities of contaminants at each tip. We observe that the energy distribution in *h*–BN is broader than that in $Si_3N_4$.

The effect of substrate thickness on a plasmonic resonance can be evaluated qualitatively by performing calculations. We can observe the trend of the substrate thickness by performing MNPBEM calculations on $Si_3N_4$ layers of increasing thickness (S4). As expected, the dipolar mode redshifts for thicker substrates. This trend saturates above 80 nm, where the effect can be seen as identical to that of bulk. For smaller thicknesses the resonance energy tends towards that in vacuum (2.22 eV).

Aiming to better understand the effect of the *h*–BN substrate on the plasmonic properties of the Au nanotriangles we also performed CL experiments. Such experiments on FLG and thin $Si_3N_4$ membranes have been performed in the past.[9] Our expectation was to show that the *h*–BN monolayer had little effect on the optical properties of the Au triangle, making it an ideal substrate to plasmonics. However, this does not seem to be the case. We observed that CL intensity decays as a function of electron dose. In Figure 3(a-b) a CL intensity map filtered at the plasmon wavelength peak and the CL spectra at the triangle's vertices are shown. These data were obtained from the first hyperspectral image measured on this triangle. In it, the dipolar modes sustained at the three tips have distinct intensities. A subsequent acquisition after electron irradiation on the same triangle shows reduced emission (Figure 3(c-d)). However, even after electron irradiation the dipolar modes are visible in EELS data (S5). The same intensity decay of the dipolar mode was observed for different triangles on two different but similarly-produced samples.

We have no definitive explanation for this observation and we can only speculate about its possible origin. In principle, plasmonic resonances are sufficiently robust against changes in the local dielectric environment. Energy shifts and changes of the FWHM can be observed, but not a complete suppression of the plasmonic modes. In fact, in EELS experiments the dipolar modes of the three tips have fairly equal scattering intensities and they do not visibly change in sequences of acquisitions. For this reason, we do not believe that the plasmonic mode is strongly modified by electron irradiation. A more reasonable interpretation is that electron irradiation creates non-radiative decay channels for the plasmons which: 1) were not available initially and 2) do not occur in the FLG or $Si_3N_4$ substrates. That is, it is intrinsically linked to the electron irradiation and to *h*–BN. The only mechanism we can suggest that matches these two criteria is the creation of defects by the electron beam. It is known that focused electron beams are quite effective in creating boron vacancies[36–38] and more complex defects in *h*–BN.[39] Experiments were performed with 60 and 100 keV electrons to try to distinguish some underlying difference but no clear influence of the electron kinetic energy was observed.

In conclusion, thin or monolayer *h*–BN have been demonstrated to be the best available substrates for plasmonic EELS studies. This should hold for all particles, including different materials, sustaining excitations within the bandgap of *h*–BN. However, the *h*–BN degrades CL efficiency after electron irradiation (which might not happen after photon illumination). Currently, modeling plasmon on thin substrates is not widespread. Furthermore, extensive *h*–BN monolayer grown on polycrystalline copper can be easily fabricated, making it a direct contender to $Si_3N_4$ given its better overall properties and ease of use. Finally, lithography on top of the copper/*h*–BN films is straightforward, opening the way to all the experiments available on $Si_3N_4$.

*Supplemnetary material* The Supplementary material (SM) contains information about the sample preparation, the peak fitting procedure the resonances FWHM, numerical calculations of the substrate thickness effect and the EELS data for Figure 3.

## I. ACKNOWLEDGEMENTS

This work was partially funded by National Agency for Research under the program of future investment TEMPOS-CHROMATEM with the reference ANR-10-EQPX-50. C.H. acknowledges funding from the Alexander von Humboldt Foundation through a Feodor Lynen Fellowship. Growth of hexagonal boron nitride crystals was supported by the Elemental Strategy Initiative conducted by the MEXT, Japan and the CREST (JPMJCR15F3), JST.

* luiz.galvao-tizei@u-psud.fr


1. P. Batson, Ultramicroscopy **11**, 299 (1983).
2. D. Ugarte, C. Colliex, and P. Trebbia, Phys. Rev. B **45**, 4332 (1992).
3. M. Duval Malinsky, K. L. Kelly, G. C. Schatz, and R. P. Van Duyne, The Journal of Physical Chemistry B **105**, 2343 (2001).
4. J. Nelayah, M. Kociak, O. Stéphan, F. J. G. De Abajo, M. Tencé, L. Henrard, D. Taverna, I. Pastoriza-Santos, L. M. Liz-Marzán, and C. Colliex, Nature Physics **3**, 348 (2007).
5. E. Ringe, J. M. McMahon, K. Sohn, C. Cobley, Y. Xia, J. Huang, G. C. Schatz, L. D. Marks, and R. P. Van Duyne, The Journal of Physical Chemistry C **114**, 12511 (2010).
6. K. C. Vernon, A. M. Funston, C. Novo, D. E. Gmez, P. Mulvaney, and T. J. Davis, Nano Letters **10**, 2080 (2010), pMID: 20476750.
7. C.-L. Zou, F.-W. Sun, Y.-F. Xiao, C.-H. Dong, X.-D. Chen, J.-M. Cui, Q. Gong, Z.-F. Han, and G.-C. Guo, Applied Physics Letters **97**, 183102 (2010), https://doi.org/10.1063/1.3509415.
8. F. Javier Garcia de Abajo, Review of Modern Physics **82**, 209 (2010).
9. A. Losquin, L. F. Zagonel, V. Myroshnychenko, B. Rodríguez-González, M. Tencé, L. Scarabelli, J. Förstner, L. M. Liz-Marzán, F. J. García De Abajo, O. Stéphan, and M. Kociak, Nano Letters **15**, 1229 (2015).
10. G. Li, C. Cherqui, Y. Wu, N. W. Bigelow, P. D. Simmons, P. D. Rack, D. J. Masiello, and J. P. Camden, The journal of physical chemistry letters **6**, 2569 (2015).
11. K. W. Smith, J. Yang, T. Hernandez, D. F. Swearer, L. Scarabelli, H. Zhang, H. Zhao, N. A. Moringo, W.-S. Chang, and L. M. Liz-Marzan, The Journal of Physical Chemistry C (2017).
12. S. Zhang, K. Bao, N. J. Halas, H. Xu, and P. Nordlander, Nano Letters **11**, 1657 (2011), pMID: 21410217, https://doi.org/10.1021/nl200135r.
13. S. Mazzucco, N. Geuquet, J. Ye, O. Stéphan, W. Van Roy, P. Van Dorpe, L. Henrard, and M. Kociak, Nano Letters **12**, 1288 (2012).
14. B. T. Draine, Astrophysical Journal **333**, 848 (1988).
15. F. J. García de Abajo and A. Howie, Phys. Rev. B **65**, 115418 (2002).
16. U. S. Inan and R. A. Marshall, *Numerical Electromagnetics: The FDTD Method* (2011).
17. U. Hohenester and A. Trügler, Computer Physics Communications **183**, 370 (2012).
18. P. Das and T. K. Chini, The Journal of Physical Chemistry C **116**, 25969 (2012), https://doi.org/10.1021/jp3103782.
19. N. W. Bigelow, A. Vaschillo, V. Iberi, J. P. Camden, and D. J. Masiello, ACS Nano **6**, 7497 (2012), pMID: 22849410, https://doi.org/10.1021/nn302980u.
20. Y. Cao, A. Manjavacas, N. Large, and P. Nordlander, ACS Photonics **2**, 369 (2015), https://doi.org/10.1021/ph500408e.
21. G. Haberfehlner, A. Trugler, F. P. Schmidt, A. Horl, F. Hofer, U. Hohenester, and G. Kothleitner, Nano letters **15**, 7726 (2015).
22. A. Crut, P. Maioli, N. Del Fatti, and F. Vallée, Chemical Society Reviews **43**, 3921 (2014).
23. C. R. Dean, A. F. Young, I. Meric, C. Lee, L. Wang, S. Sorgenfrei, K. Watanabe, T. Taniguchi, P. Kim, K. L. Shepard, and J. Hone, Nature Nanotechnology , doi:10.1038/nnano.2010.172 (2010).
24. G. Kim, M. Kim, C. Hyun, S. Hong, K. Y. Ma, H. S. Shin, and H. Lim, ACS nano **10**, 11156 (2016).
25. S. Zheng, J.-K. So, F. Liu, Z. Liu, N. Zheludev, and H. J. Fan, Nano letters **17**, 6475 (2017).
26. Z. Liu, Y. Gong, W. Zhou, L. Ma, J. Yu, J. C. Idrobo, J. Jung, A. H. MacDonald, R. Vajtai, and J. Lou, Nature communications **4**, 2541 (2013).
27. L. H. Li, J. Cervenka, K. Watanabe, T. Taniguchi, and Y. Chen, Acs Nano **8**, 1457 (2014).
28. L. Scarabelli, M. Coronado-Puchau, J. J. Giner-Casares, J. Langer, and L. M. Liz-Marzan, ACS nano **8**, 5833 (2014).
29. A. Gloter, A. Douiri, M. Tence, and C. Colliex, Ultramicroscopy **96**, 385 (2003).
30. L. F. Zagonel, S. Mazzucco, M. Tenc, K. March, R. Bernard, M. Tchernycheva, L. Rigutti, F. H. Julien, R. Songmuang, and M. Kociak, Nano Letters **11**, 568 (2011).
31. R. F. Egerton, *Electron Energy-Loss Spectroscopy in the Electron Microscope*, 3rd ed. (Springer, Berlin, 2011).
32. F. P. Schmidt, H. Ditlbacher, F. Hofer, J. R. Krenn, and U. Hohenester, Nano Letters **14**, 4810 (2014).
33. E. P. Bellido, A. Manjavacas, Y. Zhang, Y. Cao, P. Nordlander, and G. A. Botton, ACS Photonics **3**, 428 (2016).
34. A. Campos, A. Arbouet, J. Martin, D. Gérard, J. Proust, J. Plain, and M. Kociak, ACS Photonics (2017), 10.1021/acsphotonics.7b00204.
35. M. Bosman, E. Ye, S. F. Tan, C. A. Nijhuis, J. K. Yang, R. Marty, A. Mlayah, A. Arbouet, C. Girard, and M. Y. Han, Scientific Reports **3**, 1 (2013).
36. A. Zobelli, A. Gloter, C. P. Ewels, G. Seifert, and C. Colliex, Phys. Rev. B **75**, 245402 (2007).
37. J. H. Warner, M. H. Rmmeli, A. Bachmatiuk, and B. Bchner, ACS Nano **4**, 1299 (2010), pMID: 20148574, https://doi.org/10.1021/nn901648q.
38. K. Suenaga, H. Kobayashi, and M. Koshino, Phys. Rev. Lett. **108**, 075501 (2012).
39. O. Cretu, Y.-C. Lin, M. Koshino, L. H. G. Tizei, Z. Liu, and K. Suenaga, Phys. Rev. Lett. **114**, 075502 (2015).

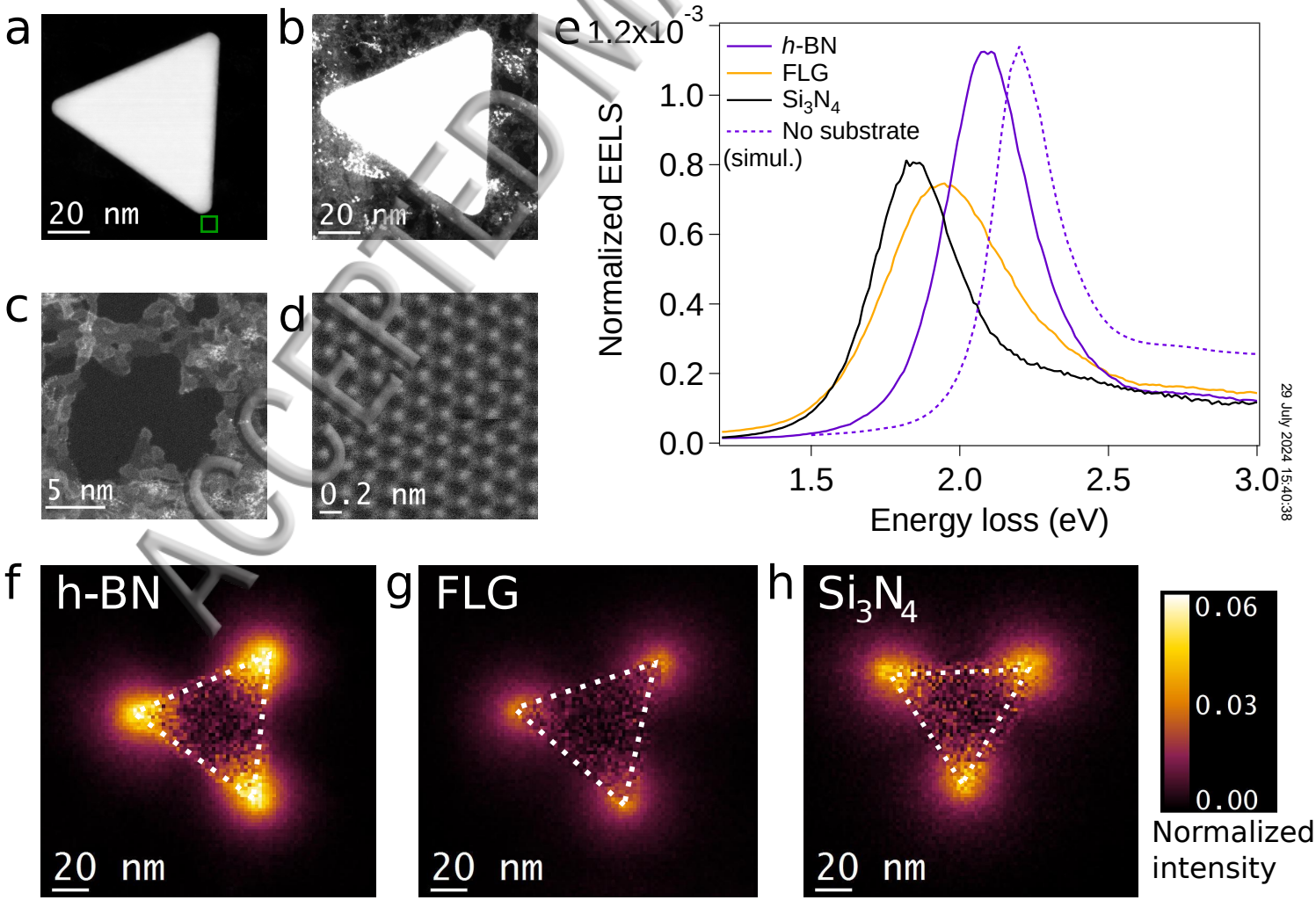

a

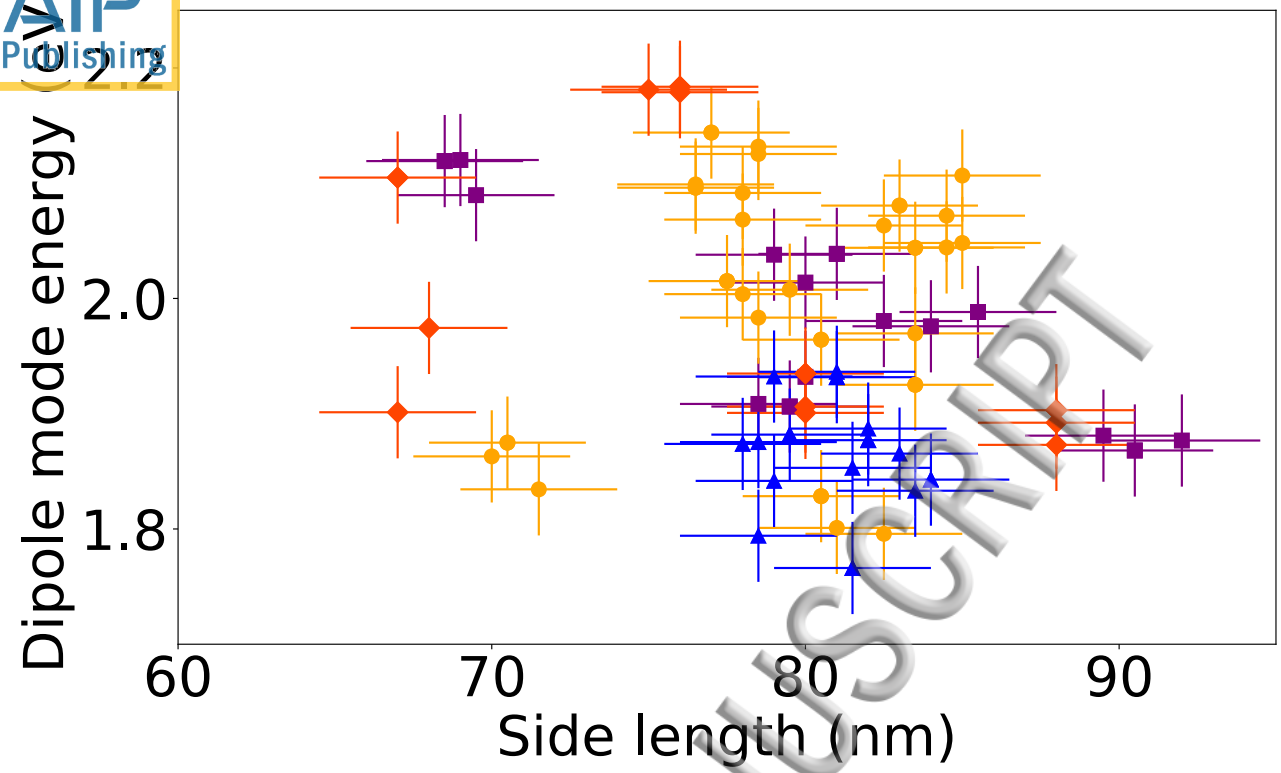



b

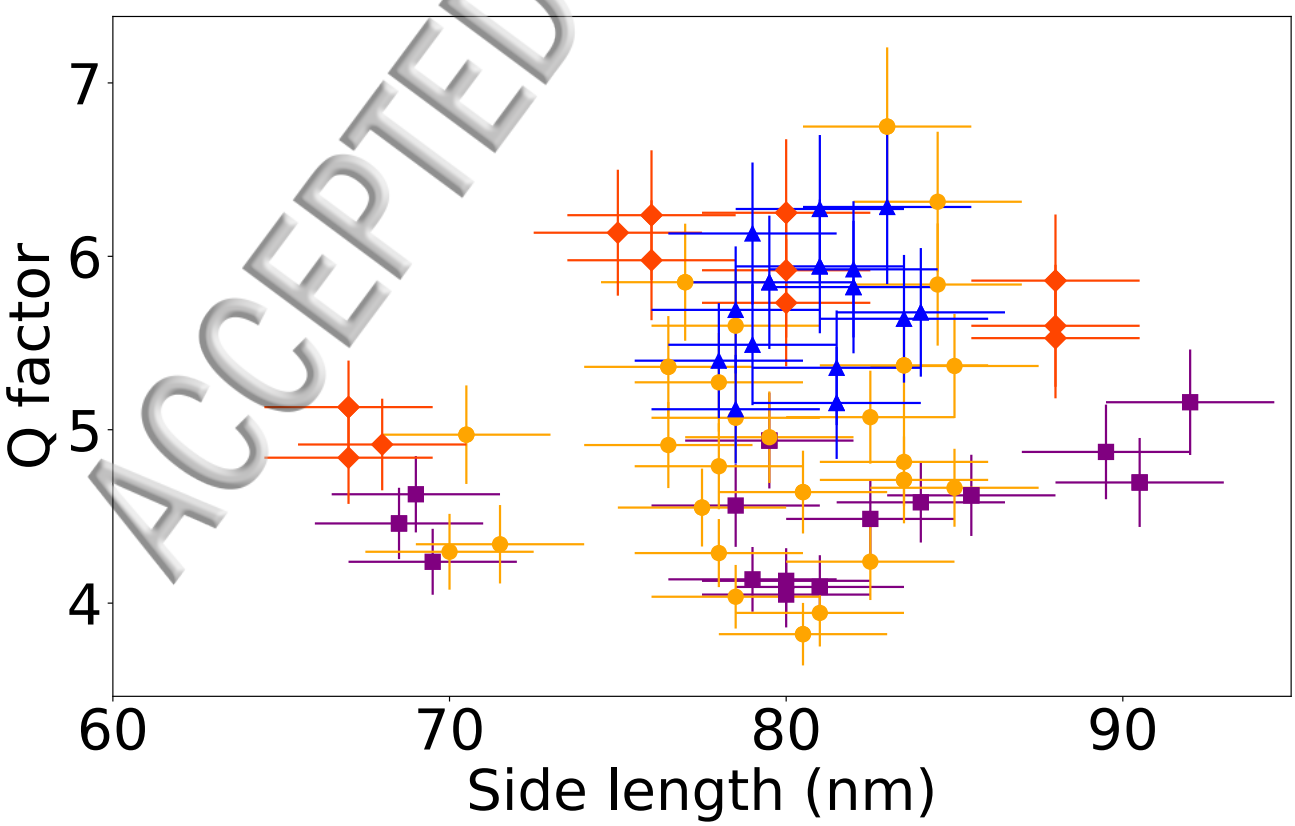

a

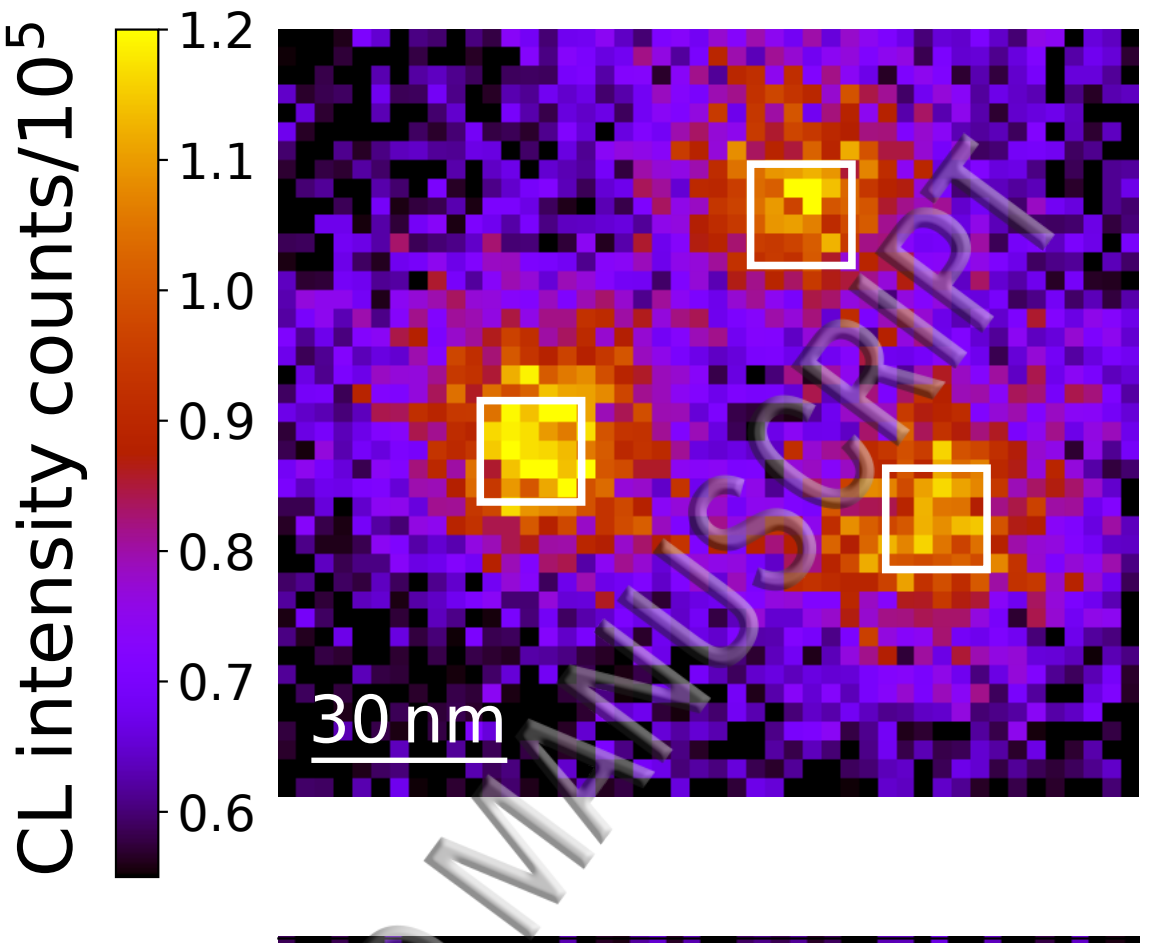


b

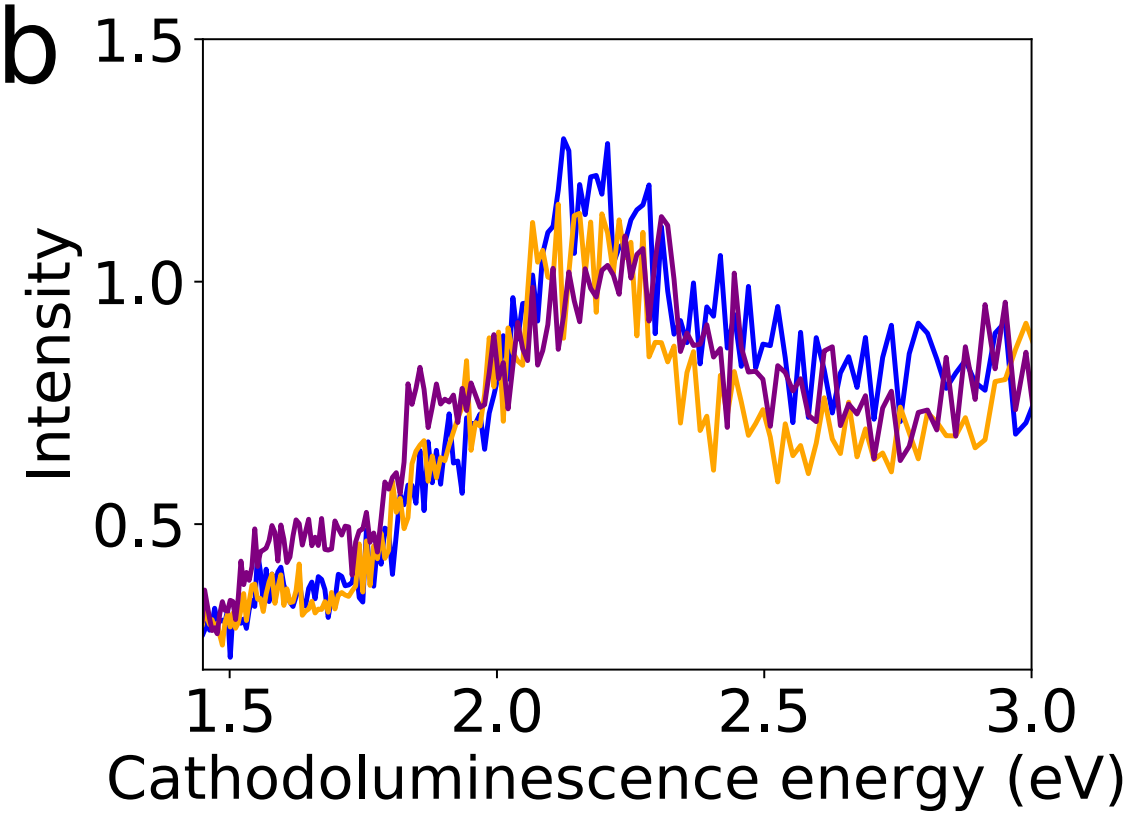


c

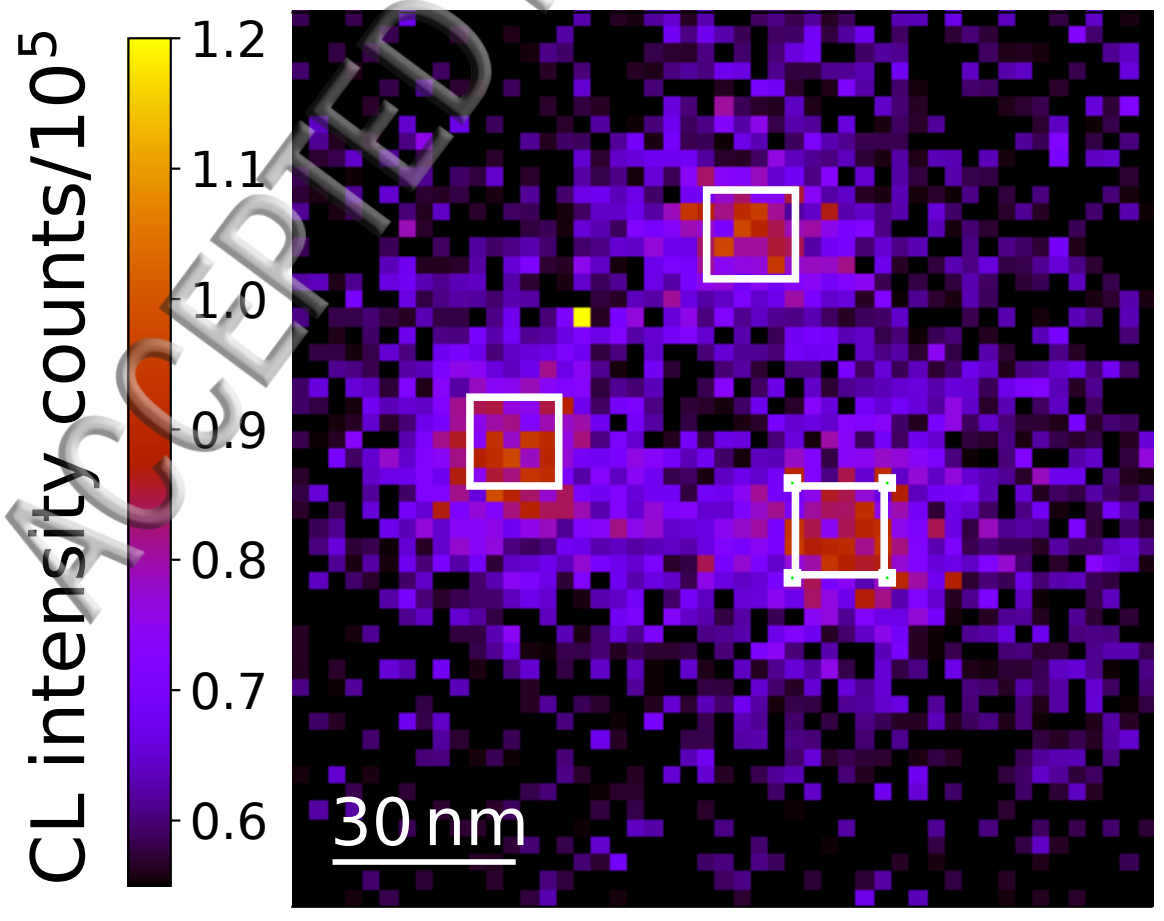


d